Supporting Information

Enhancing Electrostatic Potential Difference of High Entropy Perovskite Fluorides by Ligand Modification for Promoted Dynamic Reconstruction

Zeyu Hao[a,1], Zhengyan Du[a,1], Ting Deng[a], Dong Wang[a], Yi Zeng[a], Shansheng Yu[a], Zeshuo Meng[a,*], Xiaoying Hu[b,*], Xiufeng Hao[c,*], Hongwei Tian[a,*]

[a] Key Laboratory of Automobile Materials of MOE and School of Materials Science and Engineering, Jilin University, Changchun, 130012, China
[b] College of Science and Laboratory of Materials Design and Quantum Simulation, Changchun University, Changchun 130022, China
[c] Department of Polymer Science, College of Chemistry, Jilin University, Changchun 130012, China
E-mail: mengzs21@mails.jlu.edu.cn (Z.S. Meng); huxy@ccu.edu.cn (X.Y. Hu); haoxf@jlu.edu.cn (X.F. Hao); tianhw@jlu.edu.cn (H.W. Tian).

[1] These authors contributed equally to this work.

Figure S1 SEM images of (a-b) HEPF, (c-d) HEPF-100, (e-f) HEPF-200, and (g-h) FNS-300.

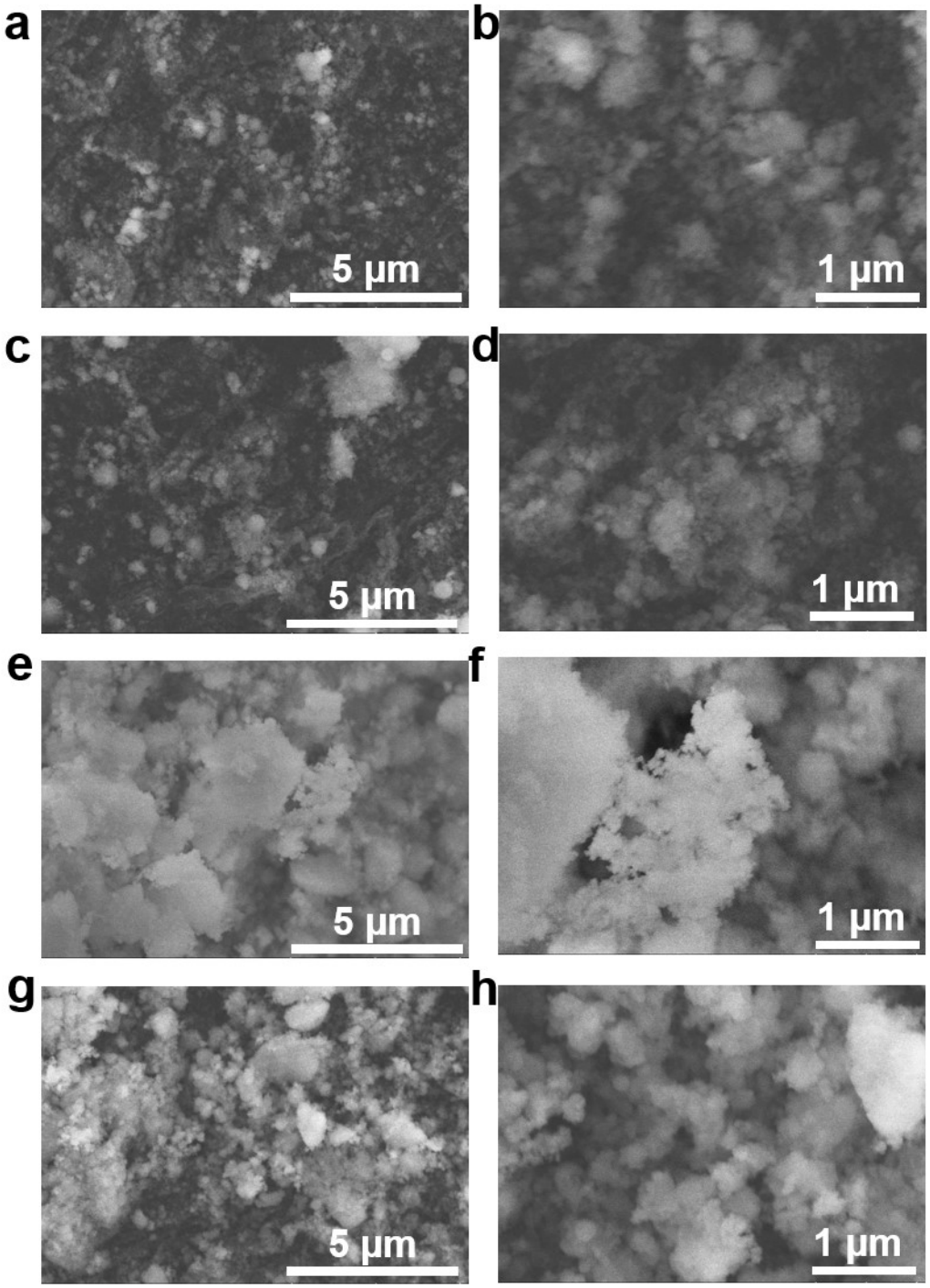

Figure S2 SEM energy dispersive spectrum (EDS) mappings of HEPF.

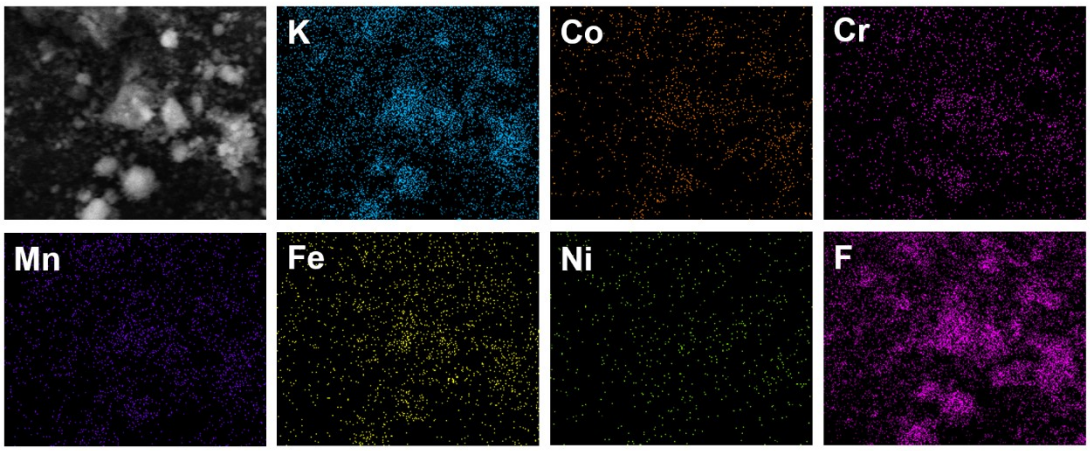

Figure S3 EDS mappings of HEPF-100.

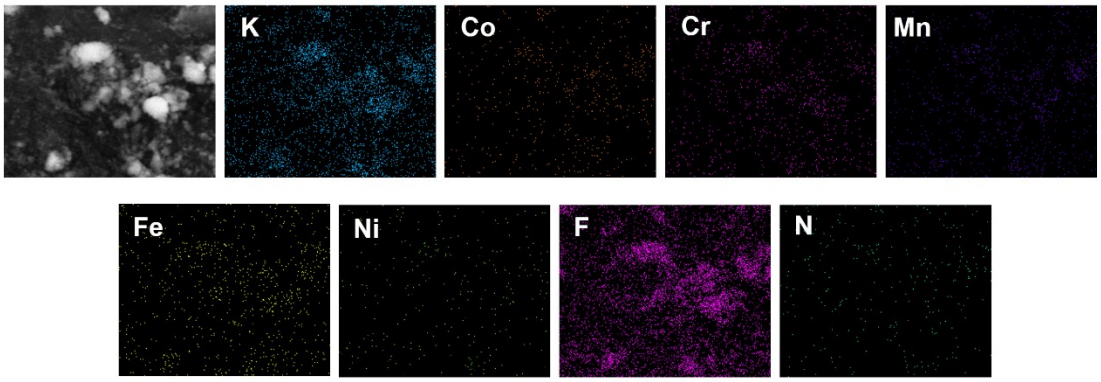

Figure S4 EDS mappings of HEPF-200.

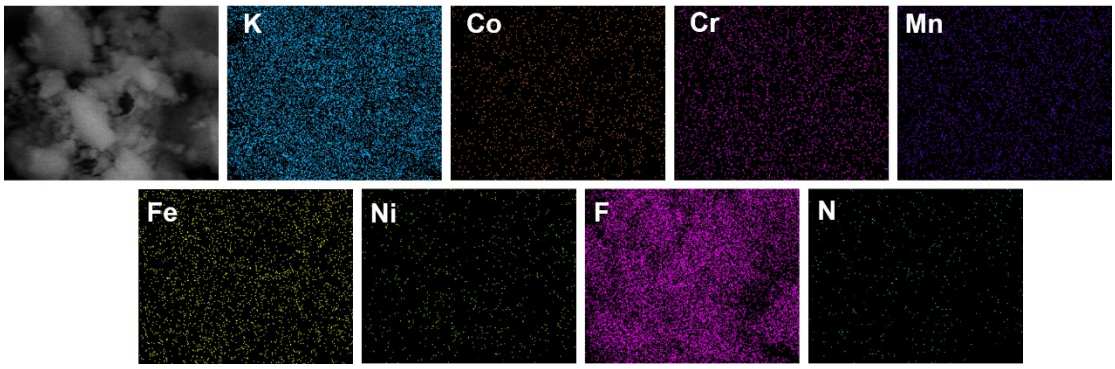

Figure S5 EDS mappings of HEPF-300.

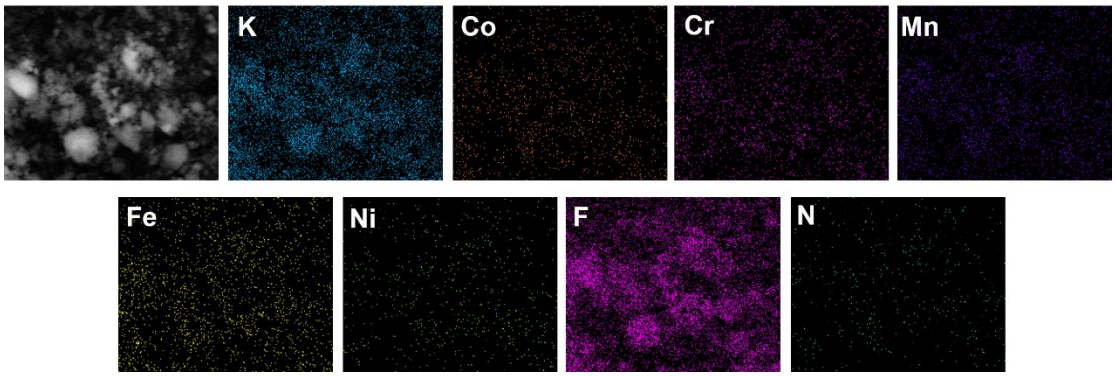

Figure S6 N_2 adsorption-desorption isotherms of (a) HEPF, (b) HEPF-100, (c) HEPF-200, and (d) HEPF-300. The corresponding pore size distributions of (e) HEPF, (f) HEPF-100, (g) HEPF-200, and (h) HEPF-300.

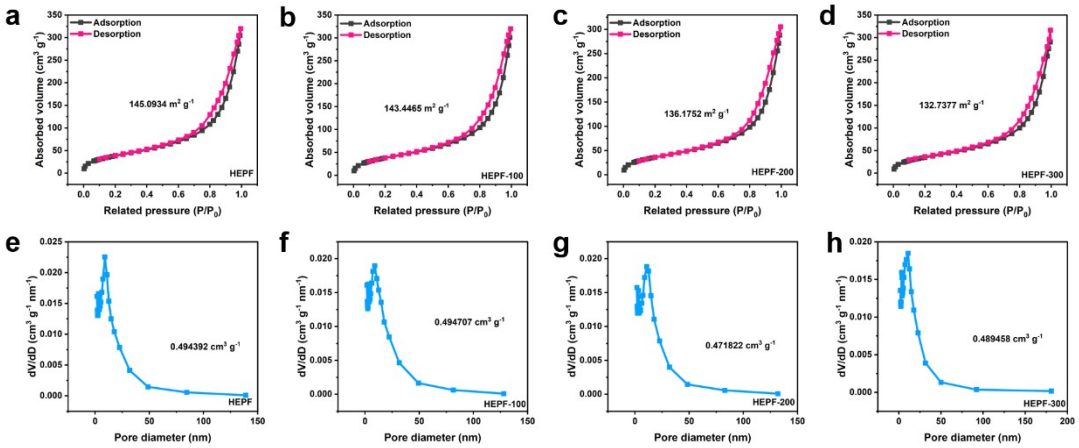

Figure S7 (a) The XPS survey scan of HEPF, and HEPF-X (X=100, 200, 300). XPS spectra of (b) K 2p for HEPF, and HEPF-X (X=100, 200, 300). (c) XPS spectra of (b) N 1s for HEPF-X (X=100, 200, 300).

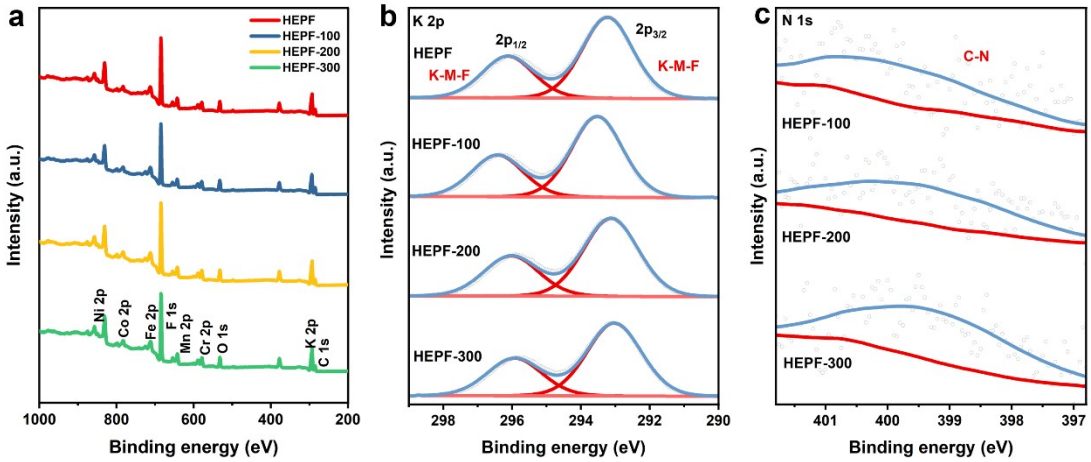

Figure S8 XPS spectra of (a) Co 2p, (b) Cr 2p, (c) Fe 2p, (d) Mn 2p, (e) Ni 2p, and (f) F 1s for HEPF-100 and HEPF-300.

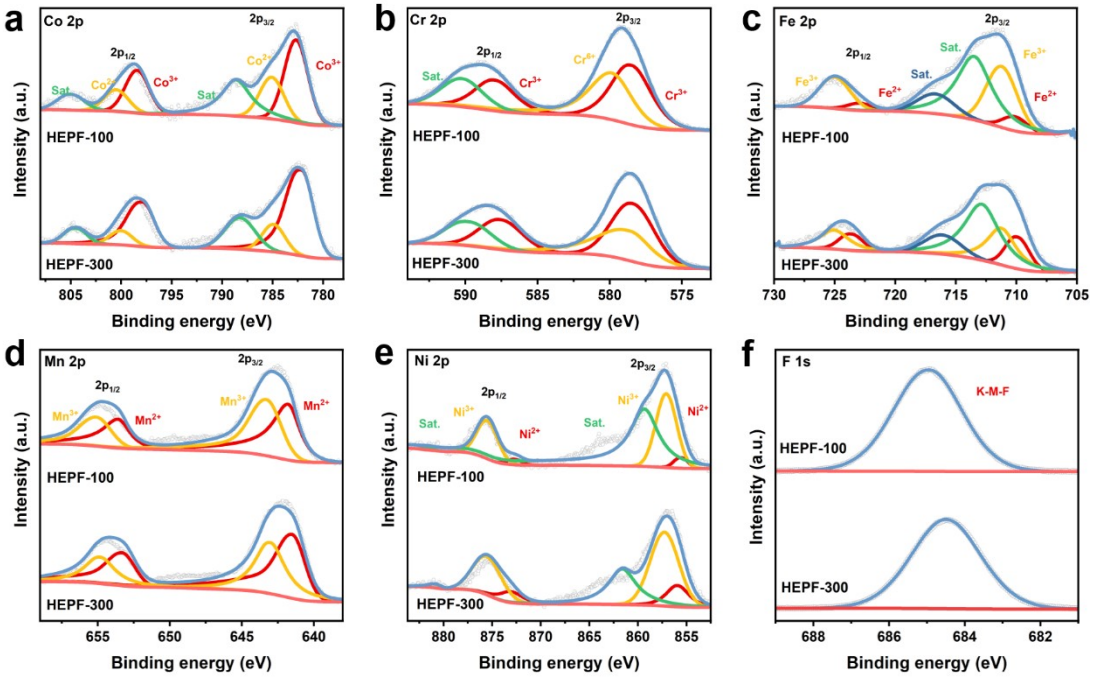

Figure S9 CV measurements for C_{dl} of (a) HEPF, (b) HEPF-100, (c) HEPF-200, and (d) HEPF-300.

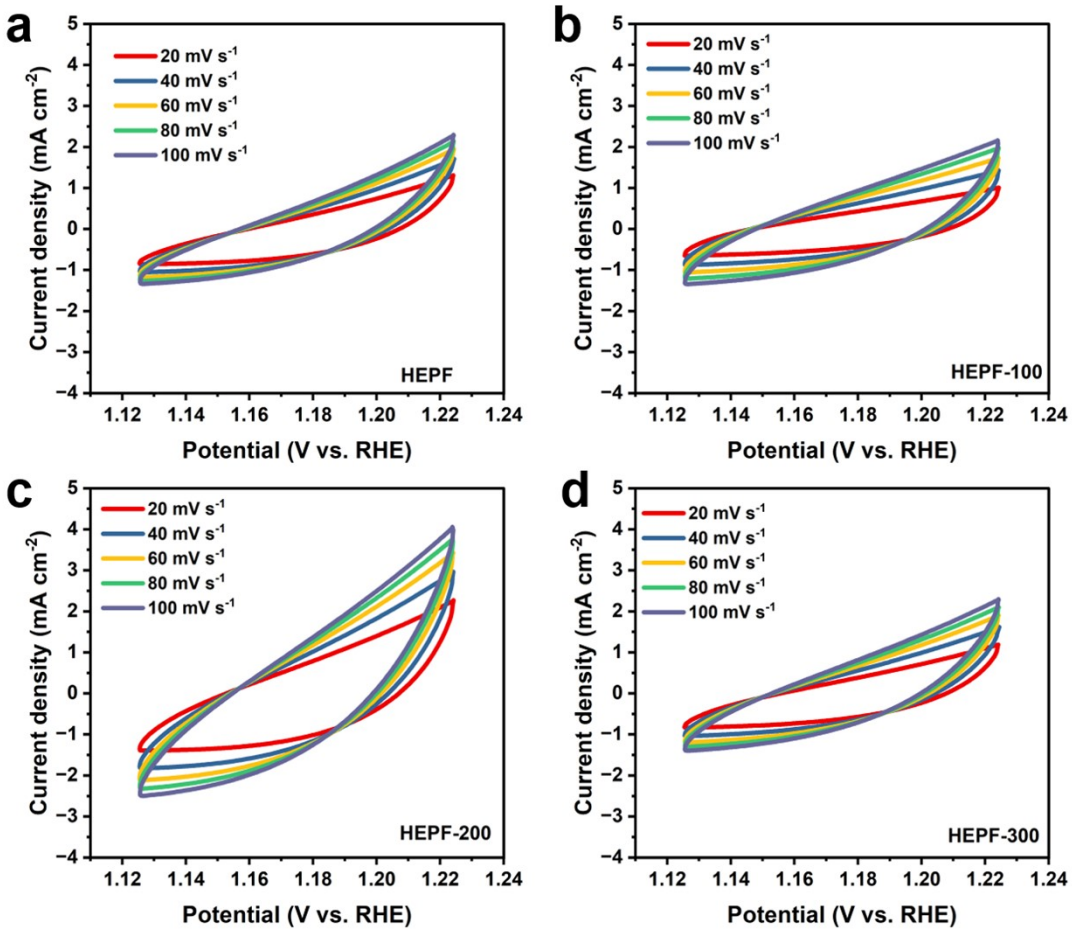

Figure S10 The normalized LSV curves of HEPF, HEPF-100, HEPF-200, and HEPF-300 catalysts based on the ECSA.

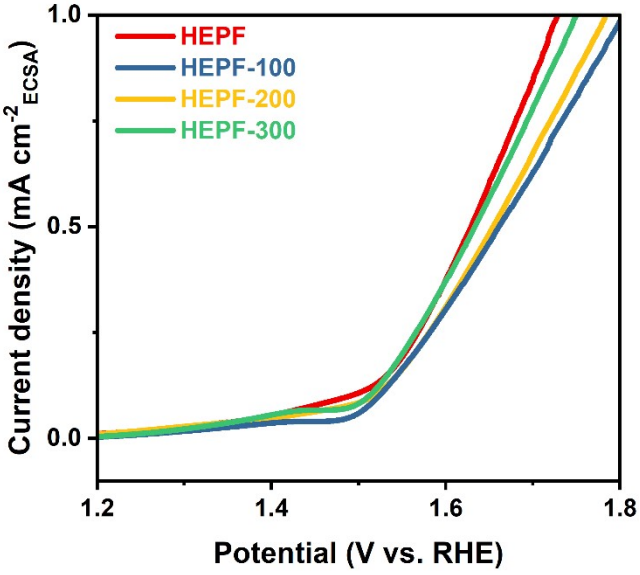

Figure S11 (a) CVs of different samples in pH=7 phosphate buffer solution at a scan rate of 50 mV s^{-1}. LSV curves normalized by (b) TOF.

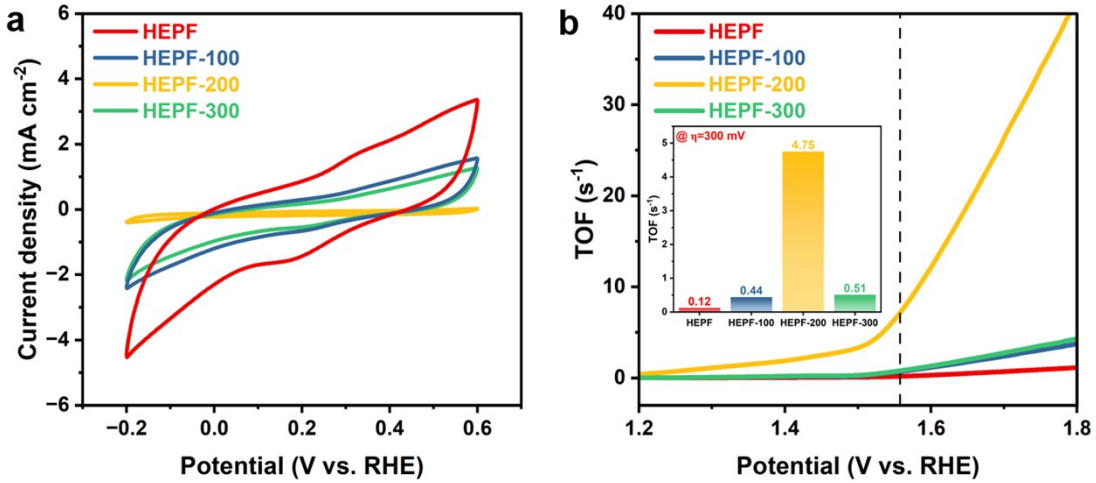

The absolute components of voltammetry charges (cathodic and anodic) were obtained from the CV curves at potentials of -0.2 V to 0.6 V vs. RHE in pH=7 phosphate buffer solution (PBS) at 50 mV s^{-1}. The turnover frequency (TOF) was determined by the following equations:

$n = Q/4F$

$TOF = I/4Fn$

where I represent the current (A) during LSV measurements, Q refers to the number of voltammetry charges (C), n denotes the number of active sites (mol), and F is the Faraday constant (96500 C mol^{-1}). The factor of 1/4 in the equations represents the four electrons needed to form one oxygen molecule from two oxygen atoms.

Figure S12 Nyquist plots for (a) HEPF and (c) HEPF-200 at different applied potentials vs. RHE in 1 M KOH. Phase angle vs. log (frequency) plots of EIS data recorded at various voltages for (b) HEPF and (d) HEPF-200.

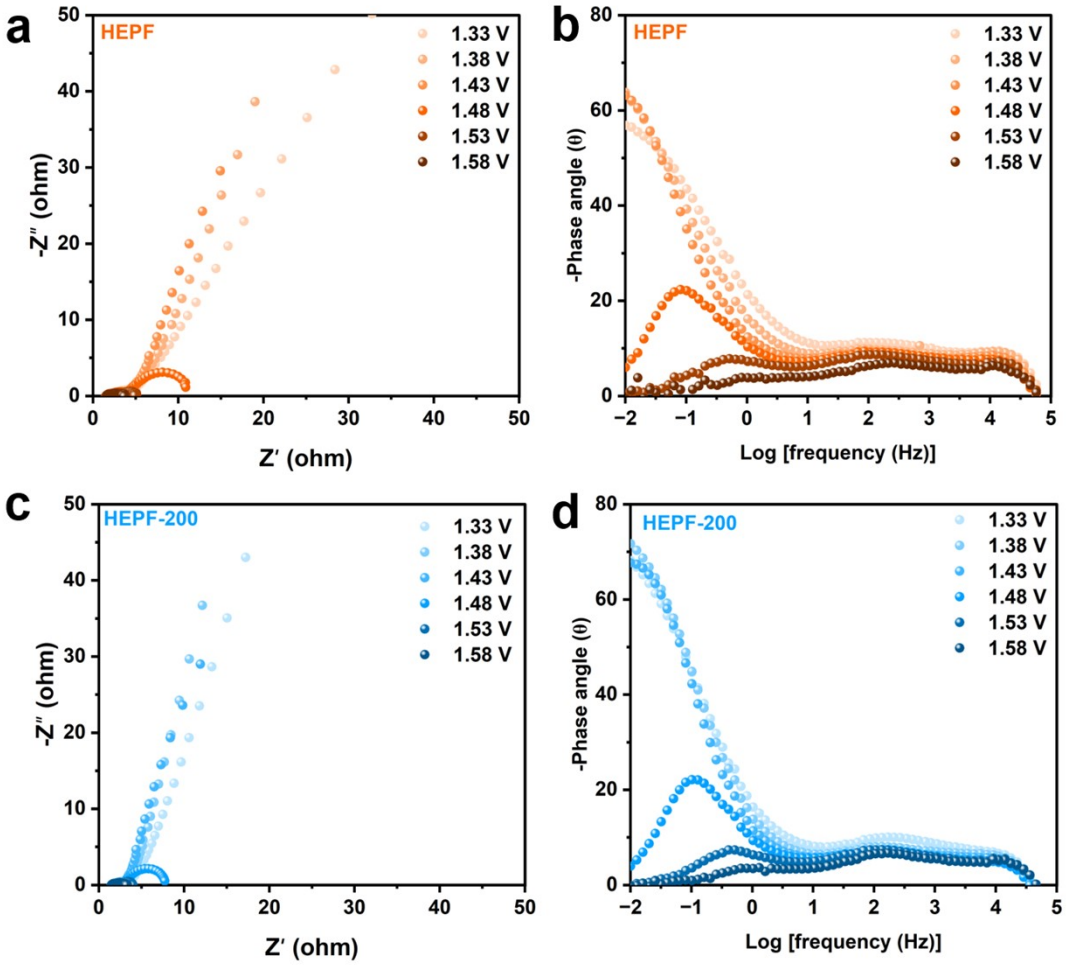

Figure S13 XRD patterns of HEPF and HEPF-200 after the chronopotentiometry stability test.

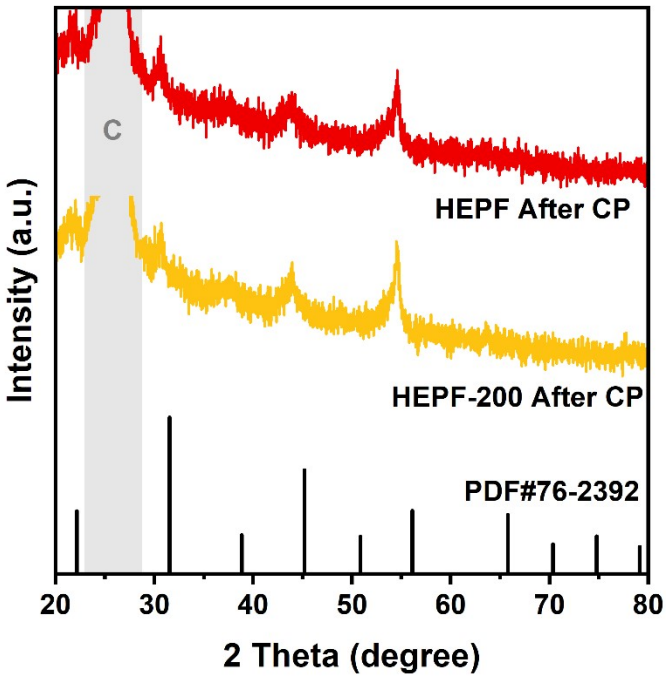

Figure S14 (a) SEM image and (b) EDS mappings of HEPF-200 after the chronopotentiometry stability test.

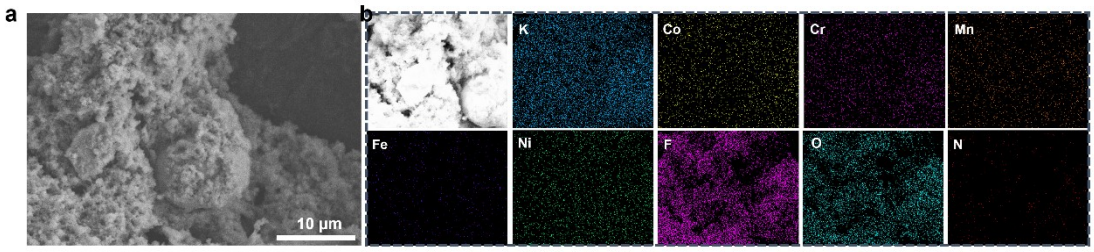

Figure S15 Raman spectroscopy for HEPF and HEPF-200 after the chronopotentiometry stability test.

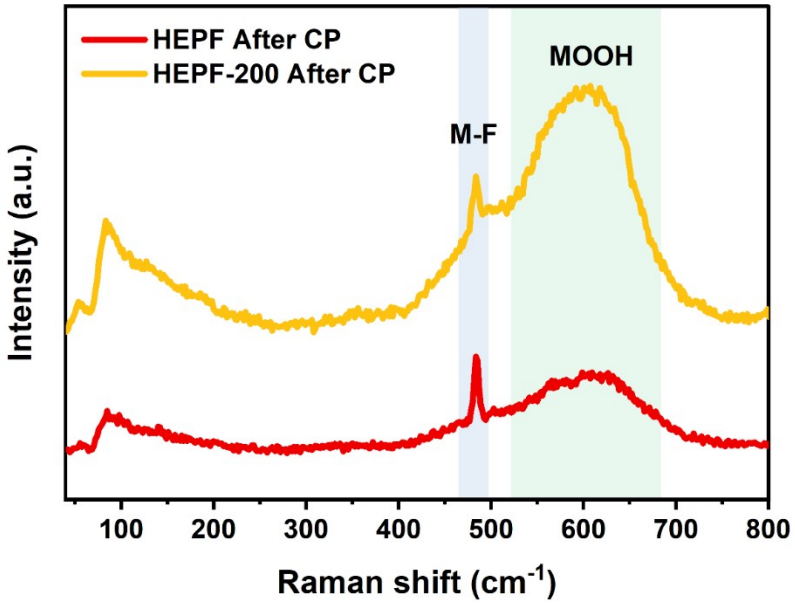

Figure S16 Co 2p XPS spectra of (a) HEPF and (b) HEPF-200 at different CV cycles. Cr 2p XPS spectra of (c) HEPF and (d) HEPF-200 at different CV cycles.

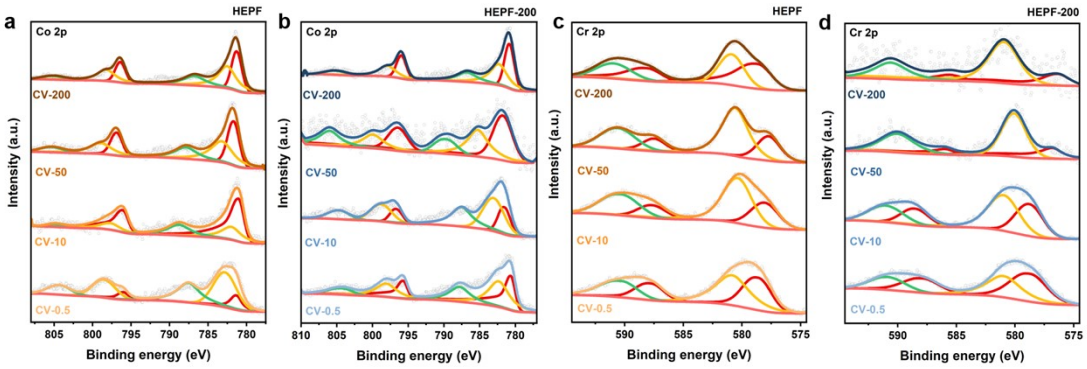

Figure S17 XPS spectra measured at different CV cycles of O 1s for (a) HEPF and (b) HEPF-200 during the OER process.

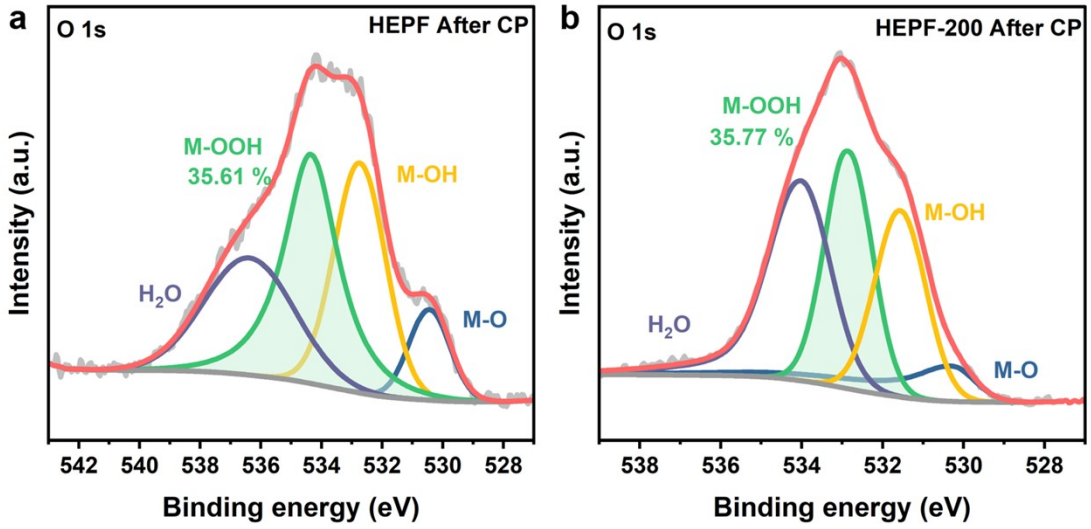

Figure S18 XRD patterns of synthesized $K(CoMnFeNiCrZnMgAl)F_3$ and $K(CoMnFeNiCrZnMgAl)F_3$-PVP.

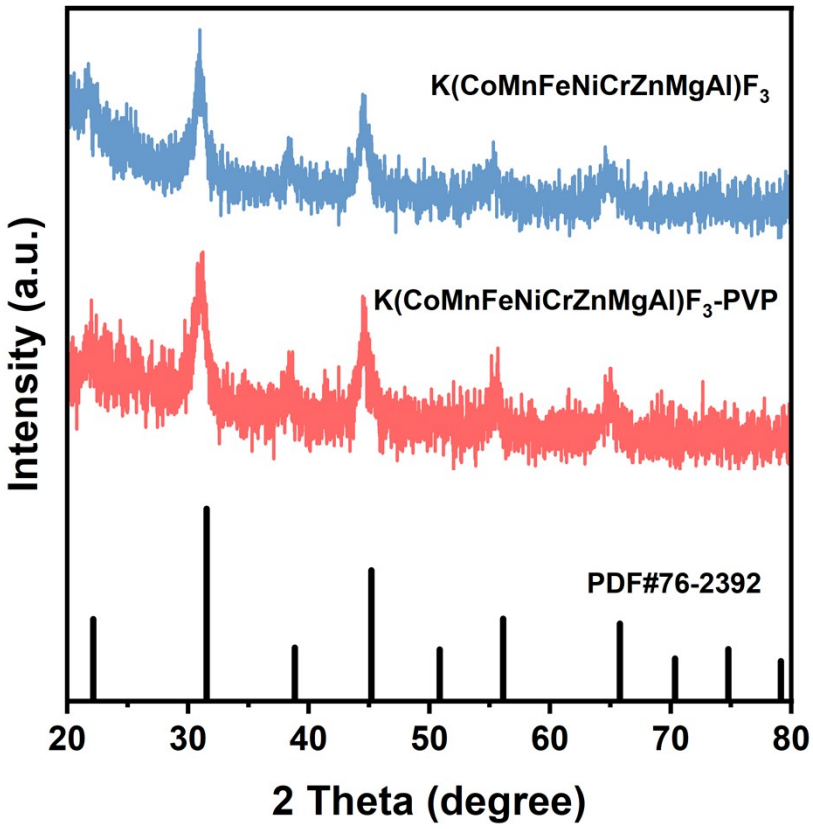

Figure S19 XPS spectra of (a) Full spectra, (b) K 2p, (c) Co 2p, (d) Mn 2p, (e) Fe 2p, (f) Ni 2p, (g) Cr 2p, (h) Zn 2p, (i) Mg 2p, (j) Al 2p, and (k) F 1s for $K(CoMnFeNiCrZnMgAl)F_3$ and $K(CoMnFeNiCrZnMgAl)F_3$-PVP. XPS spectra of (l) N for $K(CoMnFeNiCrZnMgAl)F_3$-PVP.

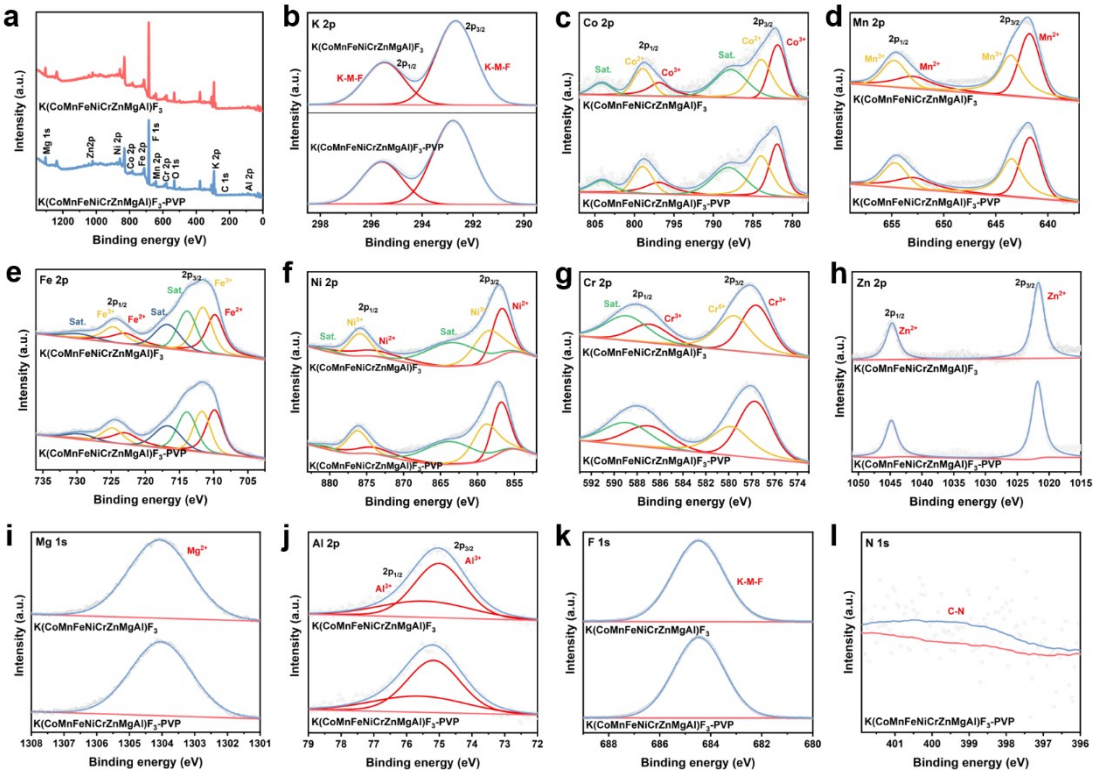

Figure S20 SEM images of (a, b) $K(CoMnFeNiCrZnMgAl)F_3$, and (c, d) $K(CoMnFeNiCrZnMgAl)F_3$-PVP.

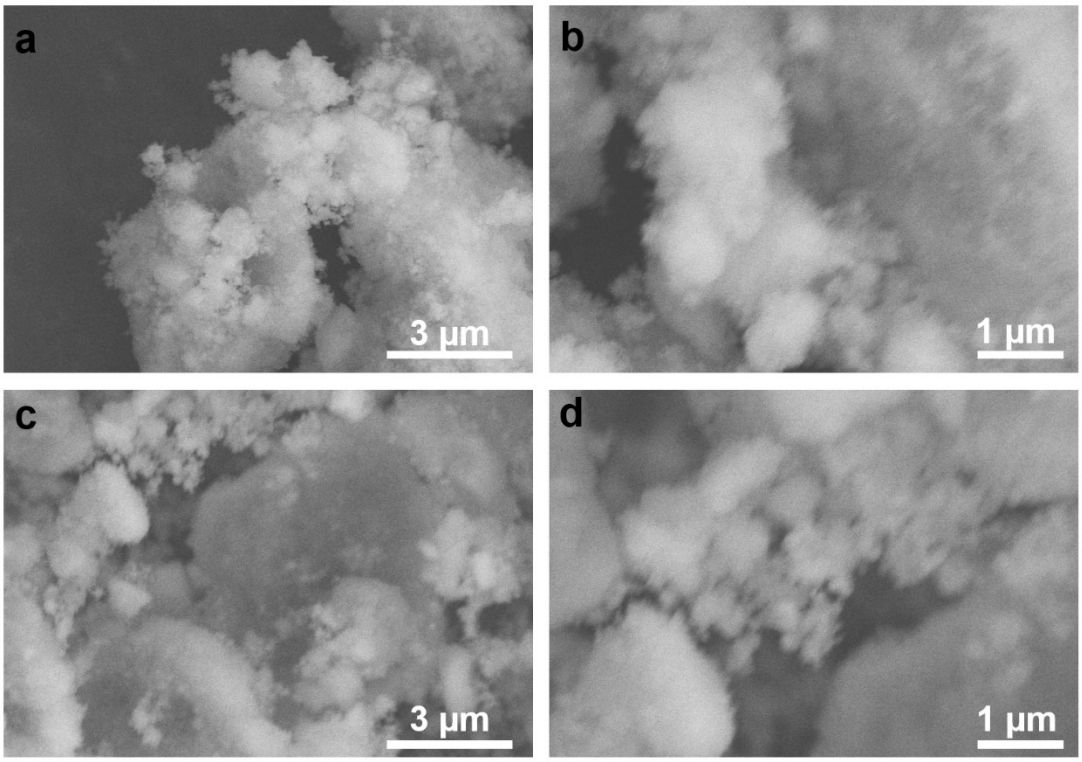

Figure S21 EDS mappings of $K(CoMnFeNiCrZnMgAl)F_3$.

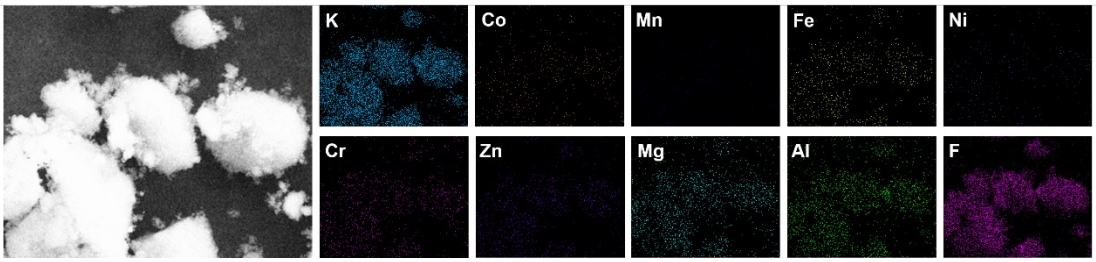

Figure S22 EDS mappings of K(CoMnFeNiCrZnMgAl)F_3-PVP.

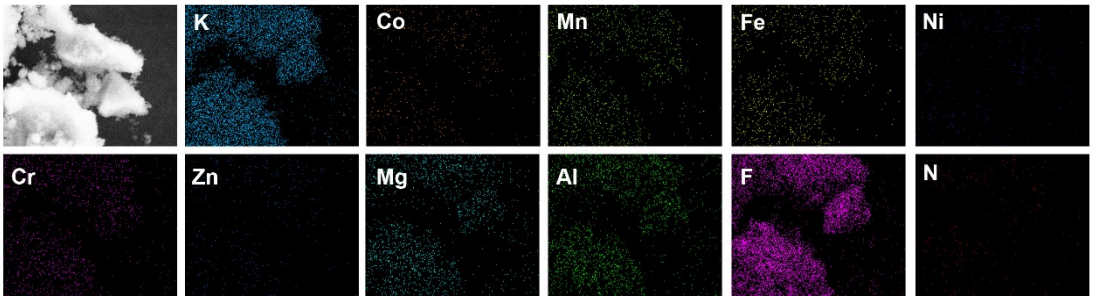

Figure S23 Raman spectroscopy of $K(CoMnFeNiCrZnMgAl)F_3$ and $K(CoMnFeNiCrZnMgAl)F_3$-PVP.

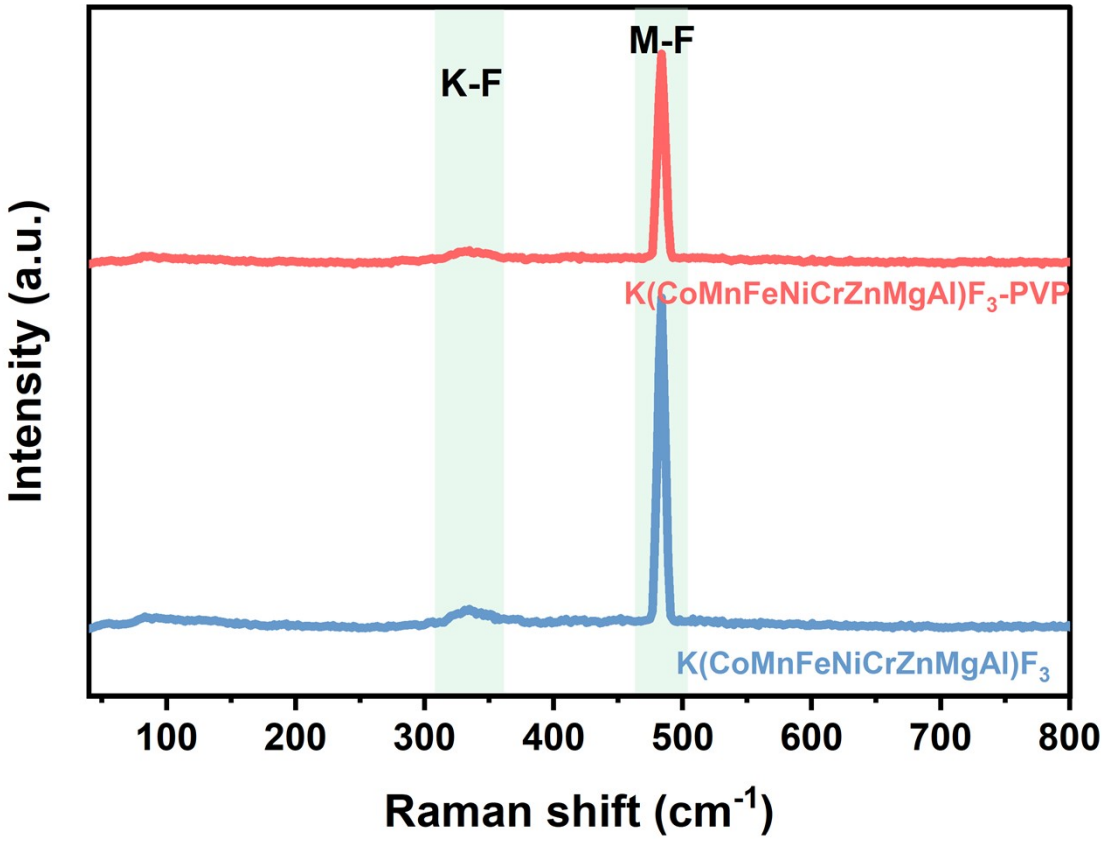

Figure S24 (a) LSV curves, (b) EIS of different samples, and (c) Tafel slopes of K(CoMnFeNiCrZnMgAl)F_3 and K(CoMnFeNiCrZnMgAl)F_3-PVP.

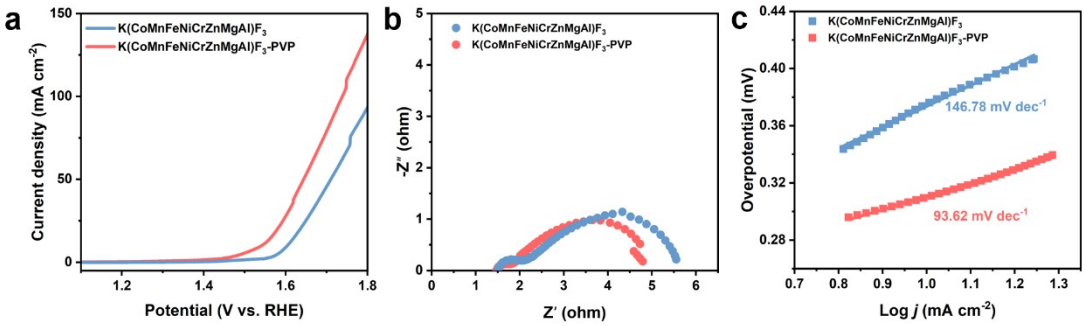

Table S1 Chemical compositions of HEPF and HEPF-X.

ID	Co [%]	Mn [%]	Fe [%]	Ni [%]	Cr [%]
HEPF	18.6	19.2	21.5	20.4	20.3
HEPF-100	19.7	18.8	20.5	21.4	19.6
HEPF-200	20.7	17.9	21.4	19.2	21.4
HEPF-300	19.2	19.6	20.2	20.6	20.4

The chemical compositions of HEPF and HEPF-X were determined by inductively coupled plasma mass spectrometry (ICP-MS). As shown in Table S1, the mole fraction of each B-site element was estimated to about 0.2, indicating a molar ratio of the five metal elements at the B-site of 1:1:1:1:1.

Since the formation of high-entropy phases is mainly driven by high configurational entropy, it can be concluded that such high configurational entropy might have originated from multi-element mixing. The molar configuration entropy of HEPF was calculated following equation:

$$S = -R\sum_{i=1}^{N} x_i \ln x_i$$

where R is the ideal gas constant and x_i is the mole fraction of the corresponding element. The molar configuration entropy was greater than 1.5 R, further proving the high-entropy nature of the synthesized HEPF material.

Table S2 The BET specific surface area and BJH pore size of different catalysts.

	Surface Area (m^2 g^{-1})	**Pore Size (cm^3 g^{-1})**
HEPF	145.09	0.49
HEPF-100	143.45	0.49
HEPF-200	136.18	0.47
HEPF-300	132.74	0.49

Table S3 The ratios of Co^{3+}/Co^{2+} in HEPF and HEPF-200.

	Co^{3+}/Co^{2+}
HEPF	2.49
HEPF-200	1.93

Table S4 C-N binding energy in the N 1s XPS spectrum of HEPF-X (X = 100, 200, 300).

Samples	**HEPF-100**	**HEPF-200**	**HEPF-300**
Binding energy/eV	399.90	399.50	399.24

Table S5 The calculation process of ECSA of HEPF, and HEPF-X (X=100, 200, 300).

Samples	C_{dl} (mF cm^{-2})	C_s (mF cm^{-2})	ECSA
HEPF	2.29	0.04	57.25
HEPF-100	4.72		118
HEPF-200	5.63		140.75
HEPF-300	3.41		85.25

Table S6 Comparison of overpotential with other OER catalysts.

Samples	Overpotential (mV)	Catalyst loading amount	Ref.
$K(MgMnFeCoNi)F_3$	397	0.7 mg cm^{-2}	[1]
$[LaM(III)O_3]_{3/4}[KM(II)F_3]_{1/4}$	345	0.7 mg cm^{-2}	[2]
$NaCo_{1-2x}Fe_xNi_xF_3$	265	0.35 mg cm^{-2}	[3]
$KNi_{0.8}Co_{0.2}F_3$	310	0.7 mg cm^{-2}	[4]
$(NH_4)_3Fe_xCo_{1-x}F_6$	243	0.2 mg cm^{-2}	[5]
HEPF-200	242	0.5 mg cm^{-2}	This work

Table S7 EIS data of HEPF and HEPF-X (X = 100, 200, 300).

	R_s (Ω)	R_{ct} (Ω)
HEPF	1.68	5.85
HEPF-100	1.63	3.91
HEPF-200	1.43	2.97
HEPF-300	1.48	4.44

Table S8 The contents of ion in electrolyte after CV activation from the ICP results.

Samples	Co	Mn	Fe	Ni	Cr
HEPF	0.0038 mg/L	0.0071 mg/L	0.0053 mg/L	0.0079 mg/L	0.0042 mg/L
HEPF-200	0.0021 mg/L	0.0095 mg/L	0.0114 mg/L	0.0071 mg/L	0.0138 mg/L

Table S9 Chemical compositions of $K(CoMnFeNiCrZnMgAl)F_3$ and $K(CoMnFeNiCrZnMgAl)F_3$-PVP.

	Co	**Mn**	**Fe**	**Ni**	**Cr**	**Zn**	**Mg**	**Al**
$K(CoMnFeNiCrZnMgAl)F_3$	11.3%	13.2%	11.5%	12.4%	11.9%	12.7%	13.4%	13.6%
$K(CoMnFeNiCrZnMgAl)F_3$-PVP	13.8%	12.6%	14.3%	12.9%	11.5%	12.7%	11.8%	10.4%

Table S10 EIS data of K(CoMnFeNiCrZnMgAl)F_3 and K(CoMnFeNiCrZnMgAl)F_3-PVP.

	R_s (Ω)	**R_{ct} (Ω)**
K(CoMnFeNiCrZnMgAl)F_3	1.51	5,71
K(CoMnFeNiCrZnMgAl)F_3-PVP	1.46	4.92

References

[1] T. Wang, H. Chen, Z. Yang, J. Liang, S. Dai, *Journal of the American Chemical Society* **2020**, *142*, 4550-4554.

[2] T. Wang, J. Fan, C.-L. Do-Thanh, X. Suo, Z. Yang, H. Chen, Y. Yuan, H. Lyu, S. Yang, S. Dai, *Angewandte Chemie-International Edition* **2021**, *60*, 9953-9958.

[3] H. Yao, Y. Zheng, S. Yue, S. Hu, W. Yuan, X. Guo, *Inorganic Chemistry Frontiers* **2023**, *10*, 804-814.

[4] S. G. Chandrappa, P. Moni, D. Chen, G. Karkera, K. R. Prakasha, R. A. Caruso, A. S. Prakash, *ACS Applied Energy Materials* **2021**, *4*, 13425-13430.

[5] Y. Li, J. Li, X. Zhai, Y. Liu, G. Wang, X. Yang, G. Ge, *ACS Applied Energy Materials* **2022**, *5*, 13981-13989.